ADVANCED MATERIALS INTERFACES
Open Access
www.advmatinterfaces.de

Ultrathin Al_2O_3 Protective Layer to Stabilize the Electrochromic Switching Performance of Amorphous WO_x Thin Films

Mario Gies, Sebastian L. Benz, Mark M. Pradja, Derck Schlettwein, Sangam Chatterjee, Martin Becker,* and Angelika Polity*

Electrochromic materials play a key role in smart windows, displays or anti-glare rear-view mirrors. Tungsten oxide is an intensely studied representative due to its extraordinary coloring performance. For commercial use, however, further optimization of the general cycle stability as well as the protection against external factors, such as moisture, is a still ongoing focus of research. In this study, the stabilization of the electrochromic switching performance of tungsten oxide is investigated using an ultrathin optimized Al_2O_3 protective coating, grown by atomic layer deposition. Amorphous tungsten oxide (a-WO_x) thin films are prepared by reactive radio-frequency sputtering. The composition as well as electronic structure of the pure a-WO_x films is studied by X-ray photoelectron spectroscopy. The electrochromic properties of the multilayer system are investigated in a nonaqueous electrolyte as well as in an electrolyte containing 10 vol% water. On the basis of these results, the stabilizing effect on the electrochromic switching characteristics of a-WO_x by the use of the additional thin Al_2O_3 protective layer is evident. It is shown that degradation and ageing of a-WO_x due to moisture can be prevented and coloration efficiencies of 50.4 $cm^2\ C^{-1}$ can be achieved at 630 nm.

1. Introduction

The need for energy saving and sustainable technologies is of increasing priority in order to counteract global climate change despite a growing population and the associated increase in primary energy demand.[1,2] Due to their diversity and versatility, transition metal oxides play a central role in energy-related applications,[3–7] such as lithium-ion batteries, supercapacitors, photo- and electrocatalysts or electrochromic (EC) devices.[8–17] In order to stabilize the oxides against undesired side reactions, thin inert protective layers can be used as shown, e.g., for cathode materials in lithium-ion batteries.[18–21] EC devices have the potential to play a key role in energy saving in the building sector, which accounts for 42 % of the European energy consumption.[22,23] For this purpose, the electrochromic effect is used in so-called smart windows. Electrochromism is based on the reversible change of optical absorption stimulated by an external voltage, which causes a redox reaction by (de-)intercalation of adequate ions (e.g., H^+, Li^+ or Na^+) of an electrolyte into the EC material. As a consequence, coloration or bleaching processes in the material occur. In general, EC materials can be categorized into two different types. One type is represented by so-called anodic EC materials, in which the deintercalation of ions causes the coloration. These include, among others, the oxides of Ni or Ir.[24] The other type is represented by cathodic EC materials. They exhibit coloration upon intercalation of ions. Typical representatives are MoO_3, or WO_3. Tungsten oxide can be considered the most established EC material, as was already mentioned by Deb in 1969 and it has been subject to intensive research ever since.[25–27] Its cathodic EC mechanism yields strong coloration upon ion intercalation. Thereby, the optical state modulates from colorless transparent to a deep blue color. This process results in the reversible formation of a tungsten bronze M_yWO_3, according to

$$\left[WO_3 + yM^+ + ye^-\right]_{\text{bleached}} \rightleftharpoons \left[M_yWO_3\right]_{\text{colored}} \quad (1)$$

M. Gies, S. L. Benz, M. M. Pradja, S. Chatterjee, M. Becker, A. Polity
Institute for Experimental Physics I
Justus Liebig University
35392 Giessen, Germany
E-mail: mario.gies@exp1.physik.uni-giessen.de;
Martin.Becker@exp1.physik.uni-giessen.de

M. Gies, S. L. Benz, M. M. Pradja, D. Schlettwein, S. Chatterjee, M. Becker, A. Polity
Center for Materials Research (ZfM/LaMa)
Justus Liebig University
35392 Giessen, Germany

D. Schlettwein
Institute of Applied Physics
Justus Liebig University
35392 Giessen, Germany

The ORCID identification number(s) for the author(s) of this article can be found under https://doi.org/10.1002/admi.202202422.

DOI: 10.1002/admi.202202422

Here, y represents the respective injected quantity of ions and electrons. As ion M^+ often H^+, Li^+ or Na^+ are intercalated.[28]

A variety of different methods can be used for the preparation of tungsten oxide. These include wet chemical synthesis methods as well as gas-phase techniques.[29–38] Depending on synthesis method and preparation parameters, the composition, crystal structure or morphology can be specifically adjusted to ensure proper function for the desired application. In terms of composition, sputter-deposited samples of near-stoichiometric tungsten oxide have a lower coloration efficiency than sub-stoichiometric tungsten oxide (WO_x, $x < 3$).[39] Sub-stoichiometric WO_x exists in a large number of stable, so-called Magnéli phases.[40] Thereby, WO_x with a ratio of $O/W > 2.5$ appears transparent and largely colorless, $O/W \simeq 2.5$ blue, and $O/W < 2.5$ shows a metallic character in color.[41] Irreversible charge transfer and coloration in the first cycle is reported for super-stoichiometric samples.[42–44] Thus, especially concerning sputtering techniques, the O_2/Ar gas flux ratio is the main adjustment screw to obtain thin films with improved electrochromism.[45–47] Just recently, Atak and co-workers addressed the variation of O_2/Ar gas flux ratio and, to a lesser extent, total pressure in DC magnetron sputtering to open up a parameter space to demonstrate WO_x thin films with suitable EC characteristics upon cycling in an 1 M lithium perchlorate ($LiClO_4$, 98%) / propylene carbonate (PC, 99%) electrolyte.[47] However, even their best samples showed degradation upon extended cycling in terms of decrease in charge capacity and higher dark-state transmittance implying lower optical modulation.

Compared to crystalline tungsten oxide, a more efficient and faster coloration mechanism is reported for amorphous tungsten oxide (a-WO_x). The less densely packed atomic structure in a-WO_x promotes ion mobility and, thus, has a beneficial effect on the coloration rate. A disadvantage, however, appears to be a reduced long-term stability as compared to the crystalline counterpart.[40] Hence, in amorphous layers there is even more need to mitigate degradation to improve the long-term cycling capabilities of devices employing such layers. Nanostructured WO_x can achieve a faster response time and good durability due to an increased surface area.[48,49] Additionally, specific improvement of the electrochromic properties can be achieved by doping. For this purpose, a variety of dopants have been reported.[36,50–61]

Besides the specific adaptation of the properties through the selected preparation method, external factors can also influence the electrochromic characteristics. For example, water can adsorb on the surface of a thin film or even diffuse into the layer structure. The influence of water is reported as the main reason for the shortening of the lifetime of WO_x due to the dissolution of the material.[62] At the same time, a water content of at least 50 ppm is required for the use of organic electrolytes in order to be able to reversibly switch evaporated WO_3.[63] Reichman and Bard demonstrated that water is incorporated into the film during electrochemical measurement and, thus, its composition is altered.[64] In particular, hydrous samples showed a significant decrease in current over the measurement period. Yoshiike et al. studied aging effects due to sample storage in humid atmosphere using an organic electrolyte.[65,66] They report a negative shift in the cathodic reaction due to hydroxylation and hydrolysis. Leftheriotis et al.[67] and Judeinstein et al.[68] found the same for tungsten oxide prepared in an aqueous sol-gel process. Here, the decreased cycle stability and faster degradation are attributed to irreversible Li^+ trapping according to the reaction[69]

$$(W-OH)+Li^+ \rightarrow (W-OLi)+H^+ \quad (2)$$

The influence of moisture and the resulting material aging is relevant for various fields of applications.[70,71] Additional coatings are used to stabilize the material and prevent aging. Among those applications, Al_2O_3 coatings are often being investigated as moisture barriers in solar cells or to improve the surface passivation of components for metal-oxide semiconductor capacitors.[20,72–76] Especially in lithium ion batteries the beneficial impact of an Al_2O_3 protective layer is ascribed to the build-up a Li–Al–O glass instead of any undesired interaction with carbonate-based electrolytes.[76–80] Realizing the close comparability of battery applications in terms of the type of ions to be transferred across the interface, Al_2O_3 is a most likely candidate as suitable protection layer.

In the present study, we evaluate the effect of an Al_2O_3 protective layer prepared by atomic layer deposition (ALD) on the electrochromic switching characteristics of a-WO_x. In the present case, the ultrathin Al_2O_3 layer prevents surface degradation of the tungsten oxide and the related loss of electrochromic switching performance as well as general electrochemical stability. Thus, we avoid the direct contact of the tungsten oxide layer with the electrolyte and bypass undesirable side reactions such as corrosion at the surface and maintain facile operation of the layers.

2. Results and Discussion

Prior to this work, WO_x samples have been prepared by radio-frequency (RF)-magnetron sputtering employing different sputter parameters, particularly different O_2/Ar gas flux ratios. In accordance to our previous work on ion-beam sputtering of WO_x,[36] layers produced under high O_2/Ar flux ratio were highly transparent, whereas below a certain threshold in the O_2/Ar flux ratio, a blue coloration of the layers occurred, implying a relatively strong oxygen deficit. Here, we restrict ourselves to the discussion of as-deposited films, grown with an O_2-gas flux of 20 sccm and an Ar flux of 30 sccm. Those layers are oxygen-deficient, yet appear still transparent.

On the basis of X-ray photoelectron spectroscopy (XPS) measurements, pristine layers show no unexpected elements apart from some surficial carbon (*cf.* XPS survey spectrum in Figure S1, Supporting Information). In-depth analysis is performed using the regions set for the W 4*f* and O 1*s* core levels (*cf.* Supporting Information, Figure S2) in the XP spectra. **Figure 1**a shows the W 4*f* core spectra of differently treated a-WO_x layers. In addition to the XPS signal of a sample in the as-deposited state, we compare samples with Li^+ intercalated at charge densities of 10, 20, 40, and 60 mC cm^{-2}, respectively. In each case, the charge is inserted by chronopotentiometry (CP). Additionally, we show the W 4*f* spectrum of a sample that has been subsequently discharged in an additional chronoamperometry (CA) step (1.5 V for 10 min) after an intercalation of 60 mC cm^{-2}. In all cases, the doublet formed by W $4f_{7/2}$ and W $4f_{5/2}$ of the W^{6+} oxidation states dominates the W 4*f* signal.

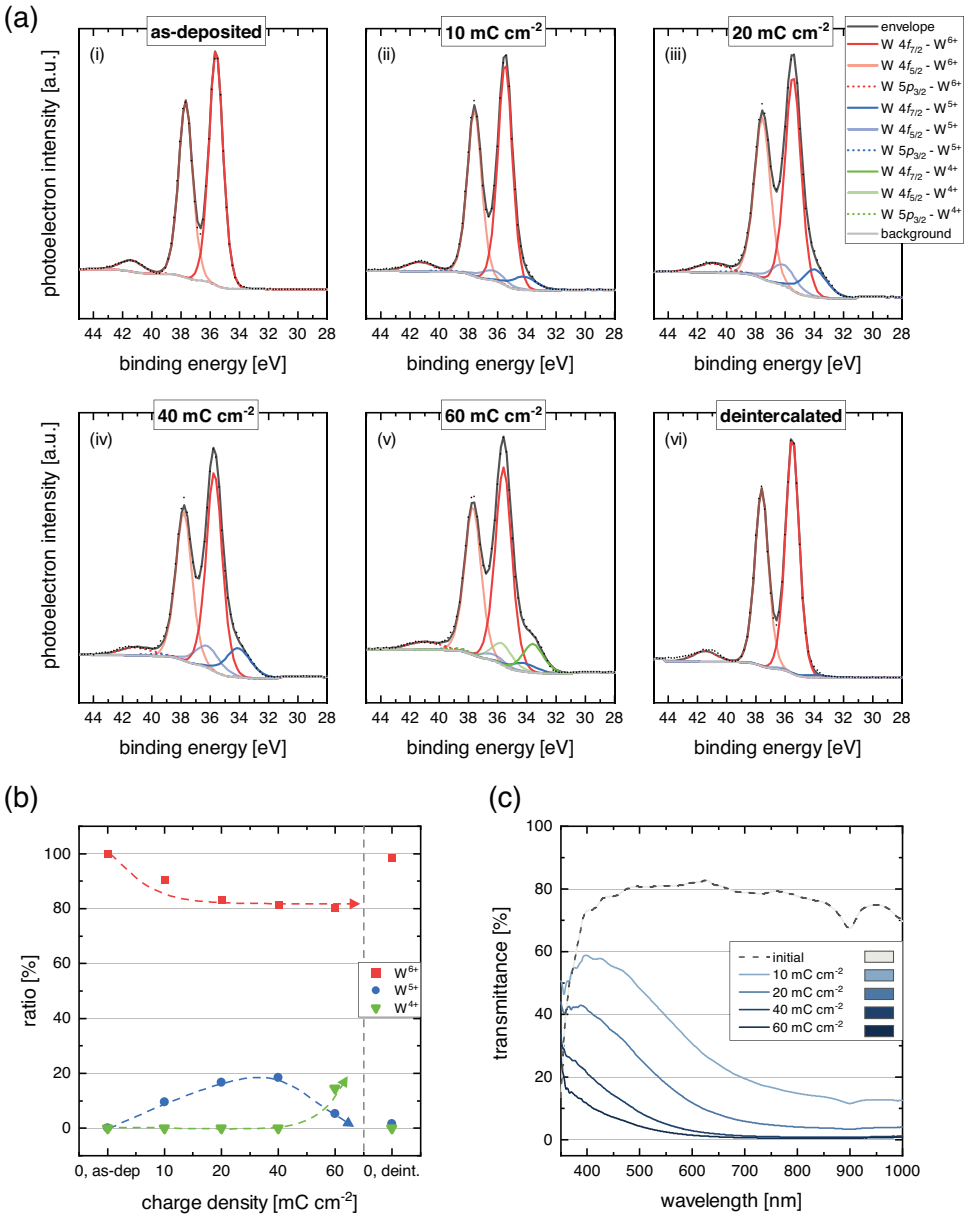

Figure 1. a-i) W 4f core level spectra of an as-deposited sample, as well as ii–v) Li^+ intercalated samples with amounts of 10, 20, 40, and 60 mC cm^{-2}, as well as vi) a final deintercalated sample. b) The shares of the oxidation states derived from the peak areas at different intercalated charge density. c) Simultaneously, the respective transmittance as well as the resulting calculated color impression (color fields in legend).

For the as-deposited sample, the former has a binding energy (BE) of about 35.6 eV.[81–84] For all presented XP spectra, the difference in spin-orbit separation of the W 4*f* corresponds to the expected $\Delta BE(W\ 4f_{5/2} - W\ 4f_{7/2}) = 2.1$ eV.[84]

In addition to the main signal of the doublet, the W $5p_{3/2}$ signal appears at higher binding energies (about 41.2 eV). However, we do not include the split signal of the W $5p_{1/2}$ in our fit due to the weakness of the W 5*p* signals. The intensity ratio of I(W $5p_{3/2}$)/ I(W $4f_{7/2}$) corresponds to a value of 0.08 for all species considered, as is also reported by Xie et al..[84] The corresponding positions of the W 4*f* and W 5*p* signals are given in **Table 1**. All fits of the tungsten species shown are performed with a mixed Gaussian/Lorentzian line-shape (%L–G = 50).

After Li^+ intercalation of 10 mC cm^{-2}, the W 4*f* signal shows an additional weak signal at lower binding energies, *cf.* Figure 1a-ii. This can be attributed to the presence of the W^{5+} species. It is formed by the reduction that takes place during the

Table 1. XPS fit parameters of different oxidation levels for the W $4f_{7/2}$ as well as for the W $5p_{3/2}$ signal.

Tungsten oxidation states	W $4f_{7/2}$ BE [eV]	W $5p_{3/2}$ BE [eV]
W^{6+}	35.6 ± 0.1	41.2 ± 0.2
W^{5+}	34.1 ± 0.1	39.7 ± 0.1
W^{4+}	33.6 ± 0.2	38.5 ± 0.2

intercalation process and accounts for about 9.5% of the total W 4*f* signal. Upon further Li^+ intercalation with charge densities of 20 and 40 mC cm^{-2}, the fraction of W^{5+} species increases to 16.7 and 18.5%, respectively. For an intercalated charge density as high as 60 mC cm^{-2}, we observe the additional signal of the W^{4+}. With a share of 14.6%, it even exceeds the W^{5+} species, which account for only 5.2%. Thus, it is reasonable to assume that reduction predominantly occurs according to $W^{5+} \rightarrow W^{4+}$ at high degrees of intercalation. For an intercalated charge density of about 20 mC cm^{-2} and above, the decreasing signal of W^{6+} shows saturation. Thus, the fraction of this species at the sample surface decreases only slightly for introduced charge densities ≥20 mC cm^{-2}. However, all procedures have in common, that the initial state can be almost completely restored by a subsequent deintercalation process carried out by CA at 1.5 V. Only a small fraction of remaining W^{5+} states appears from the W 4*f* spectrum, *cf*. Figure 1a-vi,b. Figure 1c shows the electrochromic coloration characteristics of the a-WO_x film in dependence on the charge densities. In addition to the transmittance, the optical color impression of the layer is shown as color boxes in the legend. For the untreated sample, this shows a colorless state. Accordingly, the transmittance is almost 80% across the entire visible spectral range. After an injected charge density of 10 mC cm^{-2}, a significant coloration of the sample is already visible. Here, coloration appears much stronger in the range of longer wavelengths. Hence, the maximum transmittance of less than 60% is found in the violet-blue spectral range. Further Li^+ intercalation of 20 to 40 mC cm^{-2} results in a constant decrease of the maximum transmittance (from about 15 to 20%), so that one obtains a dark blue color impression for the layer. At an intercalation level of 60 mC cm^{-2}, the transmittance is about 2.5 and 1.2% at wavelengths of 550 and 630 nm, respectively. In the subsequently presented studies of electrochromic switching performance the charge density was fixed at about ≤40 mC cm^{-2} to focus on the first reduction step of W, to study the most relevant range of transmittance changes and to safely stay in the chemically reversible range.

Figure 2a shows an SEM image of the surface of the fluorine-doped tin oxide (FTO) substrate consisting of an arbitrarily arranged, fine-grained structure consisting of increasingly sharply pointed, angular grains with an extension of up to 170 nm. For the pure a-WO_x layer, *cf*. Figure 2b, we obtain a grainy structure despite the absence of reflections in X-ray diffraction. Indicated by a rather similar number of grains per area, it can be assumed that the a-WO_x layer is influenced in its growth by the crystalline properties of the FTO substrate. However, in contrast to the morphology of the FTO substrate, the grains are round and up to 240 nm in size; some smaller grains of less than 100 nm diameter are also present. The arrangement of the grains is again arbitrary, resulting in multiple of voids. An additional, finer structure is observed on the surface of some grains.

Next, we investigate the influence of the Al_2O_3 coating on the surface morphology. Figure 2c shows the SEM image of the sample's surface with additional Al_2O_3 protective layer. The sample morphology is reproduced. Even the sub-structure of grains is still seen, showing almost perfect conformal coating of a-WO_x by an 0.75 nm thick Al_2O_3. This results in a completely comparable morphology to that of a pure a-WO_x layer.

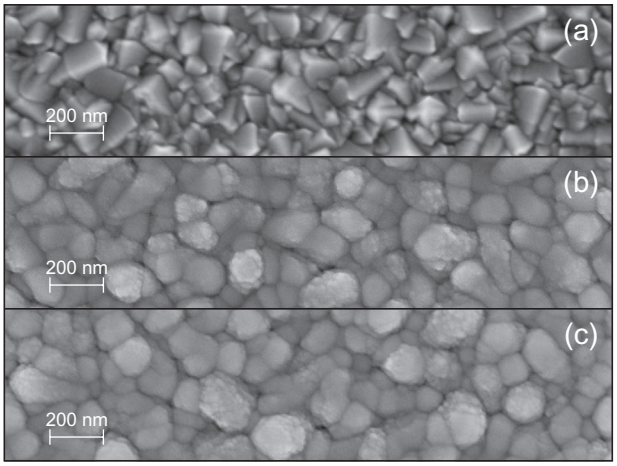

Figure 2. SEM images of a) the FTO substrate, b) a pure a-WO_x layer as well as c) the layer system Al_2O_3|a-WO_x|FTO.

In the following, we will investigate the electrochromic switching performance in order to evaluate the impact of the additional Al_2O_3 barrier. Accordingly, **Figure 3** shows the spectro-electrochemical data of a pure a-WO_x layer (a) and the Al_2O_3|a-WO_x layer system (b). Here, we use 0.75 nm of ALD-grown Al_2O_3. This thickness was chosen based on a preceding analysis of different thicknesses (not shown here), where Al_2O_3 coatings of larger thickness showed less favorable performance. Most likely there exists a critical parameter above which the additional layer significantly limits the Li^+ ion transfer into the functional WO_x layer.

All samples shown are analyzed on the basis of 100 cyclic voltammetry (CV) cycles in the voltage range between – 1.0 and 1.5 V, *cf*. Figure 3i. The arrows mark the direction of the voltage sweep. The electrochemical behavior of a pure a-WO_x sample is quite stable for the complete measurement procedure. All curves are smooth, indicating that no well-defined phase changes occur. Only the initial cycle differs significantly from the subsequent cycles, typical for conditioning during the first cycle. For the intercalation process, the highest current density of about –1.19 mA cm^{-2} is obtained at the reversal of the voltage sweep at –1.0 V.

After reaching the scan reversal point, the decrease of the intercalation current starts immediately. From about –0.81 V the deintercalation current starts. This results in a fast increase of the current density to a maximum value of almost 0.17 mA cm^{-2}. No measurable current flow is registered at the positive reversal point of the voltage sweep and the redox cycle is completed. The reversibly transferred charge density during the first cycle of measurement is 19.3 mC cm^{-2}, *cf*. Figure 3a-iv. Subsequent cycles show a slightly modified voltammogram. Here, the maximum current density of the intercalation process is – 0.95 mA cm^{-2}. The deintercalation process has a maximum current density of about 0.34 mA cm^{-2}. However, the current density is not completely zero at the positive scan reversal point. Therefore, the deintercalation reaction is not completed. The constant pattern of the CV measurements infers a high degree of stability. This is corroborated by the constant charge density of about 41 mC cm^{-2} across the whole measurement procedure, *cf*. Figure 3a-iv, even higher than in the initial cycle.

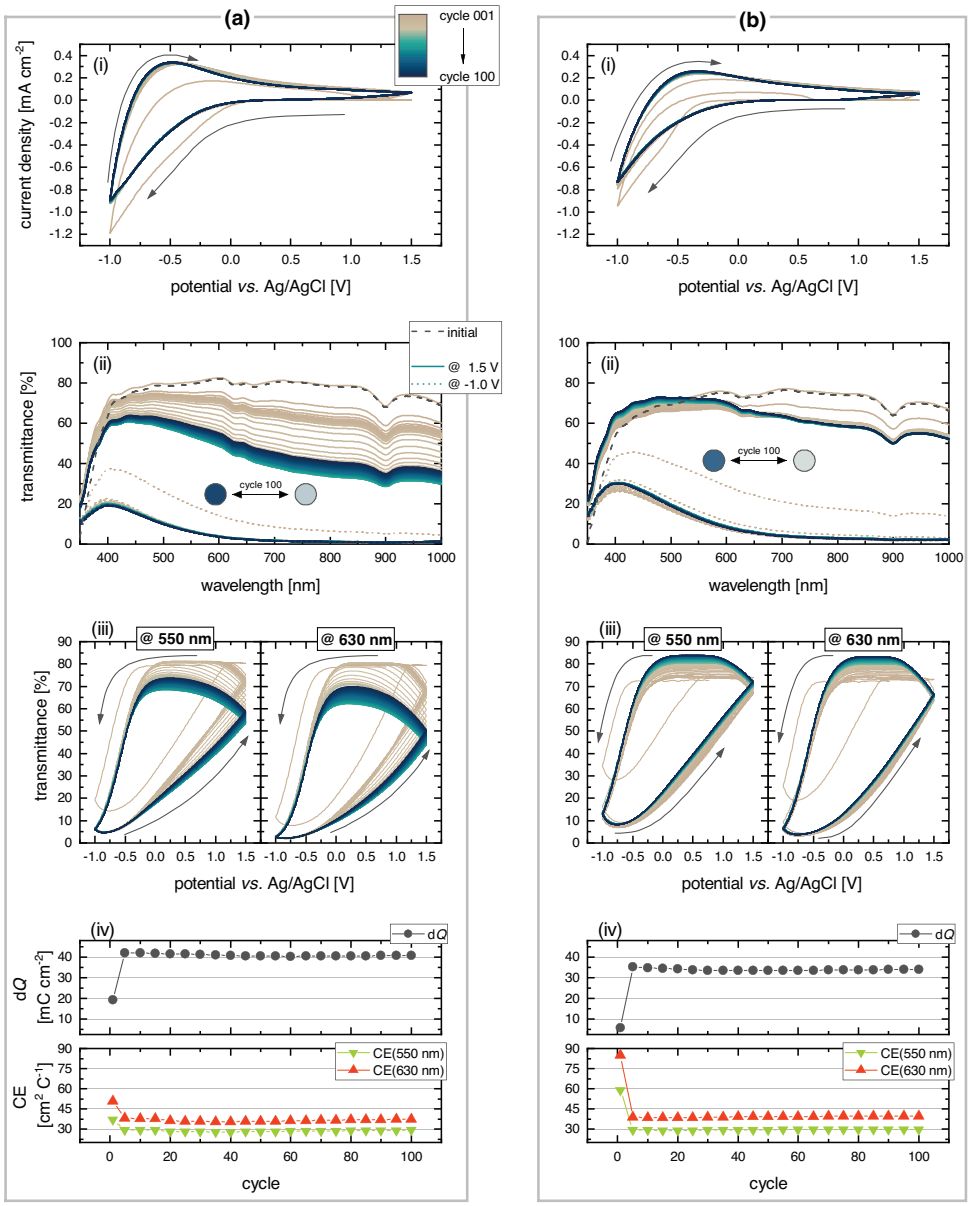

Figure 3. Spectro-electrochemical investigation on a) a pure a-WO_x sample and b) for the Al_2O_3|a-WO_x layer system in contact to 1 M $LiClO_4$ in PC. i) The electrochemical properties are investigated using 100 CV cycles between −1 and 1.5 V. ii) The optical transmittance is shown for the initial state (dashed line) as well as for the intercalated (dotted line, at −1 V) and the deintercalated state (solid line, at 1.5 V). iii) Simultaneously, the transmittance hysteresis at 550 and 630 nm is given for the entire measurement. iv) The charge density involved in the CV (upper plot) and the resulting coloration efficiency at 550 and 630 nm are shown for every fifth cycle (bottom plot).

The layer system of Al_2O_3|a-WO_x shows a comparable behavior for the electrochemical treatment, *cf.* Figure 3b-i. Generally, a slightly reduced current density is evident. The first and the second cycle again deviate slightly from the subsequent ones. The latter show a maximum current density in the range of −0.8 to −0.7 mC cm^{-2} during the intercalation process, while the deintercalation process yields a maximum current density of about 0.26 mC cm^{-2}. Compared to the pure a-WO_x sample, the layer system of Al_2O_3|a-WO_x results in a somewhat reduced charge density per cycle of about 34 mC cm^{-2}, *cf.* Figure 3b-iv. However, the Al_2O_3|a-WO_x sample shows superior stability upon electrochemical cycling. This is particularly evident when considering the transmittance behavior between 350 and 1000 nm, *cf.* Figure 3-ii. For both samples, the transmittance of their initial state (dashed line), as well as in their intercalated (dotted line, at −1 V) and in their deintercalated states (solid line, 1.5 V) is shown. Prior to measurement, both samples show a transmittance of 70 to 80% across the visible spectral range. The transmittance of the intercalated state also shows high stability for both samples. Here, the transmittance for the pure a-WO_x sample is less than 20%, whereas slightly higher values result for the Al_2O_3|a-WO_x layer system. The more intense coloration of the pure a-WO_x layer is due to the higher intercalated charge density mentioned above.

However, a significant deviation in the completeness of deintercalation of both samples is observed for transmittance measurements at a potential of 1.5 V. The initial state of the pure a-WO_x sample by far cannot be restored during electrochemical cycling. As the number of cycles increases, the transmittance of the deintercalated state continuously degrades. In particular, the first 50 cycles result in a reduction of transmittance to about 35 to 60%. Subsequent cycles results in a slight brightening; nevertheless, the final state in the visible spectral range is only about 40 to 65%. Accordingly, the optical impression changes between dark blue (at –1.0 V) and a bleached, slightly blue state (at 1.5 V), shown in Figure 3a-ii.

The transmittance of the Al_2O_3|a-WO_x layer system recorded at a potential of 1.5 V shows an opposite trend. Even though the initial state of the sample cannot be fully restored, the transmittance in the spectral range between 350 and 675 nm even improves over the measurement time. A comparison of the fourth and the last cycle shows a brightening of about 8% for the considered range. The transmittance drops only slightly (2 to 3%) with increasing number of cycles for wavelength above 675 nm. The color impression of this film is consequently modulated between a blue to a colorless light gray state for the final cycle as shown in Figure 3b-ii. Thus, the Al_2O_3|a-WO_x film system clearly demonstrates superior switching behavior compared to the pure a-WO_x sample.

To underline this finding, Figure 3iii illustrates the cyclic change of the optical transmittance at a wavelength of 550 and 630 nm in dependence of applied voltage for both types of samples. For the pure a-WO_x, the curves obtained for both wavelengths are comparable. Upon scan reversal at –1.0 V, the maximum coloration is not yet completely achieved. This occurs at a potential of –0.85 V. Here, for 550 and 630 nm, the transmittance is less than 5 or 2%, respectively. The coloration is fully reproducible for all subsequent cycles. During deintercalation, a considerably slower change of transmittance is seen than during coloration. Even at 1.5 V, bleaching of the sample is not completed yet. After passing the positive scan reversal, the first cycles show an ongoing increase in transmittance until they reach saturation at about 1 V. We end up with a transmittance of about 81%. However, a decrease in brightening is evident for later cycles. Thus, the transmittance curves are still increasing up to about 0 V, when the next intercalation starts. Consequently, the sample can no longer be fully bleached under the present cycling conditions. Notably, the samples can be regenerated by subsequent chronoamperometry, *cf.* Figure S3 (Supporting Information). Thus, only the switching rate of the layer decreases. As a result, the time of deintercalation during present cyclic voltammetry is not sufficient, so that the intercalated ions cannot be completely removed from the layer.

For the layer system of Al_2O_3|a-WO_x, a comparable transmittance profile is observed in the direction of intercalation. Again, the maximum coloration or decolorization occurs considerably later than the scan reversal. The most colored states at 550 and 630 nm have a transmittance of about 8 and 4%, respectively, for all cycles and occur at about –0.75 V. For deintercalation, however, we observe distinct differences compared to the pure a-WO_x layer. First, the saturated transmittance range is clearly evident in all cycles. Moreover, the values of maximum transmittance increase with cycle number and finally reach a value of almost 85% at both 550 and 630 nm at the latest at 0.5 V. A comparison of the completely colored and completely bleached states of the films as well as a discussion of underlying kinetics is provided in *cf.* Figure S4 (Supporting Information).

Figure 3iv gives the coloration efficiency (CE) resulting from the spectro-electrochemical measurements for every fifth cycle for 550 and 630 nm, respectively in addition to the charge density involved per cycle. The coloration efficiencies develop almost identically for both samples and indicate good operation of the films throughout this electrochemical analysis. The high stability of the determined values should be emphasized. The coloration efficiency of a pure a-WO_x after passing the 100^{th} cycle is ≈29.1 $cm^2\ C^{-1}$ (at 550 nm) or 37.3 $cm^2\ C^{-1}$ (at 630 nm). The combined Al_2O_3|a-WO_x layer system yields slightly higher values of CE(550 nm) = 29.7 $cm^2\ C^{-1}$ and CE(630 nm) = 39.5 $cm^2\ C^{-1}$, both calculated for the 100th cycle. This observation is in line with literature, although the overall values slightly differ as Li et al. evaluate CE at 670 nm.[85]

As our cycling experiment does not show any decline in charge capacity in the first 100 cycles, we are quite optimistic that an additional layer of Al_2O_3 of optimized thickness does indeed not degrade the electrochromic performance of a-WO_x. Apart from a somewhat weaker and slower coloration, the Al_2O_3|a-WO_x sample demonstrates identical coloration efficiency and faster bleaching, leading to more balanced charging-discharging kinetics and improved cycling stability under the chosen conditions. However, in the future more extended cycling has to be performed to further support our findings.

The degradation of oxides caused by external factors is often studied with the help of environmental chambers.[86,87] Here, the samples are exposed to particular conditions (e.g., relative humidity, temperature, etc.) for a predefined period of time. Based on this approach, the influence of different levels of external factors on the aging process of the sample can be evaluated. For our approach, we choose a high moisture content of our electrolyte to simulate extremely harsh conditions. However, in the smart window application, this case may occur over a longer period of time even with small leakages. If an additional Al_2O_3 layer shows a stabilizing effect under these conditions, we are rather confident that degradation of the tungsten oxide layer can be prevented even under moderate moisture conditions.

The effect of moisture is investigated to fully exploit the advantage of the Al_2O_3|a-WO_x layer system compared to a pure a-WO_x sample. **Figure 4** shows a set of spectro-electrochemical data comparable to that in Figure 3, however, with water (10 vol%) added to the organic electrolyte. In order to prevent possible decomposition of the water component, the CV measurements are carried out in a potential range, between –0.6 and 1.0 V.

The CV of the pure a-WO_x sample shows a significantly increased cathodic current density of about –1.29 mA cm^{-2} for the initial cycle, even before reaching the reversal voltage, *cf.* Figure 4a-i. For the following anodic current, on the other hand, the maximum current density achieved is comparable to the values obtained for the subsequent cycles in the range of 0.25 mA cm^{-2}. This difference in current densities within the first cycle points at a strongly irreversible process. Con-

sequently, only a small charge density of about 7 mC cm^{-2} can be reversibly (de-)intercalated within the first cycle, *cf.* Figure 4a-iv. Subsequent cycles yield largely comparable voltammograms for both shape and recorded current densities. The maximum current density of the intercalation process is –0.47 mA cm^{-2}, measured at scan reversal. Deintercalation current densities remain in the range of the initial cycle. However, the peak position shifts towards a more negative voltage. A rather constant charge density of about 12 mC cm^{-2} is obtained for the remaining cycles, *cf.* Figure 4a-iv.

In contrast, the CV of the layer system of Al_2O_3|a-WO_x exhibits more constant characteristics. The sample shows a quite similar shape of CV data as measured in the electrolyte without additional water, *cf.* Figure 4b-i versus Figure 3b-i. Maximum current densities of –0.4 mA cm^{-2} and 0.18 mA cm^{-2} are found for the intercalation and deintercalation process, respectively. The charge density increases slightly from cycle to cycle, leading to about 10 mC cm^{-2} reversibly transferred in the final cycle, *cf.* Figure 4b-iv. It should be noted that smaller charge densities are involved in the measurements in contact to the water-containing electrolyte, caused mainly by the adapted voltage range and in part perhaps by a slightly decreased Li^+- concentration.

The transmittance characteristics of the pure a-WO_x film displays a mild coloration at –0.6 V for the initial cycles, which, however, is deepened in subsequent cycles, *cf.* Figure 4a-ii. Simultaneously, the transmittance of the deintercalated state at 1.0 V switches back to the initial state or even slightly higher for the first 15 cycles. In later cycles, however, the transmittance in the bleached state continuously decreases. A similar trend is seen for the transmittance of the intercalated state, leading to a color change from gray-blue at –0.6 V to beige-brown at 1.0 V in the final cycle.

In contrast, the layer system of Al_2O_3|a-WO_x shows considerably more stable optical switching characteristics over all cycles, *cf.* Figure 4b-ii. In particular, the bleached state shows a quite constant transmittance of about 80%. Very weak coloration is obtained at –0.6 V for the initial cycles. The contrast increases significantly in the subsequent cycles. During the final cycle, the color impression of the sample changes between light blue at –0.6 V and colorless-transparent at 1.0 V, *cf.* Figure 4b-ii.

Coloration of the pure a-WO_x film intensifies cycle by cycle as shown for the transmittance at 550 and 630 nm. The transmittance decreases to about 23% at 550 nm and 15% at 630 nm, *cf.* Figure 4a-iii. The transmittance in the bleached state, however, continuously decreases, leading to 51% at 550 nm and 59% at 630 nm in the final cycle. Overall, a strong degradation of the sample leading to a small contrast between bleached and colored state is evident.

The Al_2O_3|a-WO_x layer system, on the other hand, shows an increase in optical contrast between the two states over the entire course of the measurements stemming from quite constant transmittance of the bleached state and progressively smaller transmittance in the colored state that results in a transmittance of about 38% at 550 nm and 25% at 630 nm in the final cycle, *cf.* Figure 4b-iii. The minimum transmittance is reached slightly after scan reversal, indicating slightly smaller intercalation through the Al_2O_3 layer. In contrast, the bleaching process is largely completed even before the respective scan reversal. For both wavelengths considered, a transmittance of more than 85% can be observed over all cycles.

The calculated coloration efficiencies shown in Figure 4iv are very similar for both samples. The switching is even more efficient for both samples compared to the previous measurement in the purely organic electrolyte, *cf.* Figure 3iv. This is due to the relatively small charge density involved, which, nevertheless, ensures a comparably intense optical switching as reflected in the higher coloration efficiency. Constancy of the coloration efficiency is especially outstanding for the Al_2O_3|a-WO_x layer system. Although the charge density increases constantly over the time of measurement for this sample, the coloration efficiency stays at a constant level of CE(550 nm) = 34.3 cm^2 C^{-1} and CE(630 nm) = 50.4 cm^2 C^{-1} in the 100th cycle.

The coloration efficiency obtained for the Al_2O_3|a-WO_x sample and, in particular, the high degree of reversibility reached in the switching characteristics of this layer system in the water-containing electrolyte indicate the superior stability of Al_2O_3|a-WO_x over pure a-WO_x. We emphasize that the sample with the additional Al_2O_3 protective layer does not show any signs of degradation under these conditions. In contrast, the pure a-WO_x film irreversibly degrades upon extended cycling in the presence of water, and a recovery of a bleached state with suitable color neutrality cannot be achieved.

3. Conclusion

We deposit widely amorphous tungsten oxide films using RF-magnetron sputtering and investigate the fundamental electronic properties. Despite their sub-stoichiometry, we obtained colorless, transparent samples. Films with different degrees of electrochemically intercalated Li^+ ions are investigated by X-ray photoelectron spectroscopy. Reduced tungsten species W^{5+} and W^{4+} produced during the electrochemical treatment can be identified. Furthermore, the general electrochromic switching performance of the a-WO_x films is investigated using cyclic voltammetry and chronoamperometric measurements. Over 100 CV cycles, a decrease in the transmittance in the bleached state is observed. To stabilize the electrochromic properties, an additional, ultrathin Al_2O_3 layer is deposited by ALD on top the a-WO_x films. This Al_2O_3|a-WO_x layer system exhibits significantly improved stability to the electrochemical treatment. We obtain a charge density of about 34 mC cm^{-2} per cycle combined with a coloration efficiency of around 29.7 cm^2 C^{-1} at 550 nm and 39.5 cm^2 C^{-1} at 630 nm. Additionally, we emphasize a beneficial effect against the influence of water. For this purpose, a water content of 10 vol% was added to the electrolyte. In general, a rapid degradation of pure a-WO_x is observed during the electrochemical treatment in CV with such water-containing electrolyte, which is mainly evident in an increasing deterioration of the bleached state. In contrast, the Al_2O_3|a-WO_x layer system shows its superiority in a stable electrochromic switching performance. We obtain a coloration efficiency of 34.3 cm^2 C^{-1} at 550 nm and 50.4 cm^2 C^{-1} at 630 nm for the 100th cycle, respectively. The superiority of such combined Al_2O_3|a-WO_x layer system and its stabilizing effect concerning long-term electrochromic switching may become a key factor for future concepts of electrochromic devices.

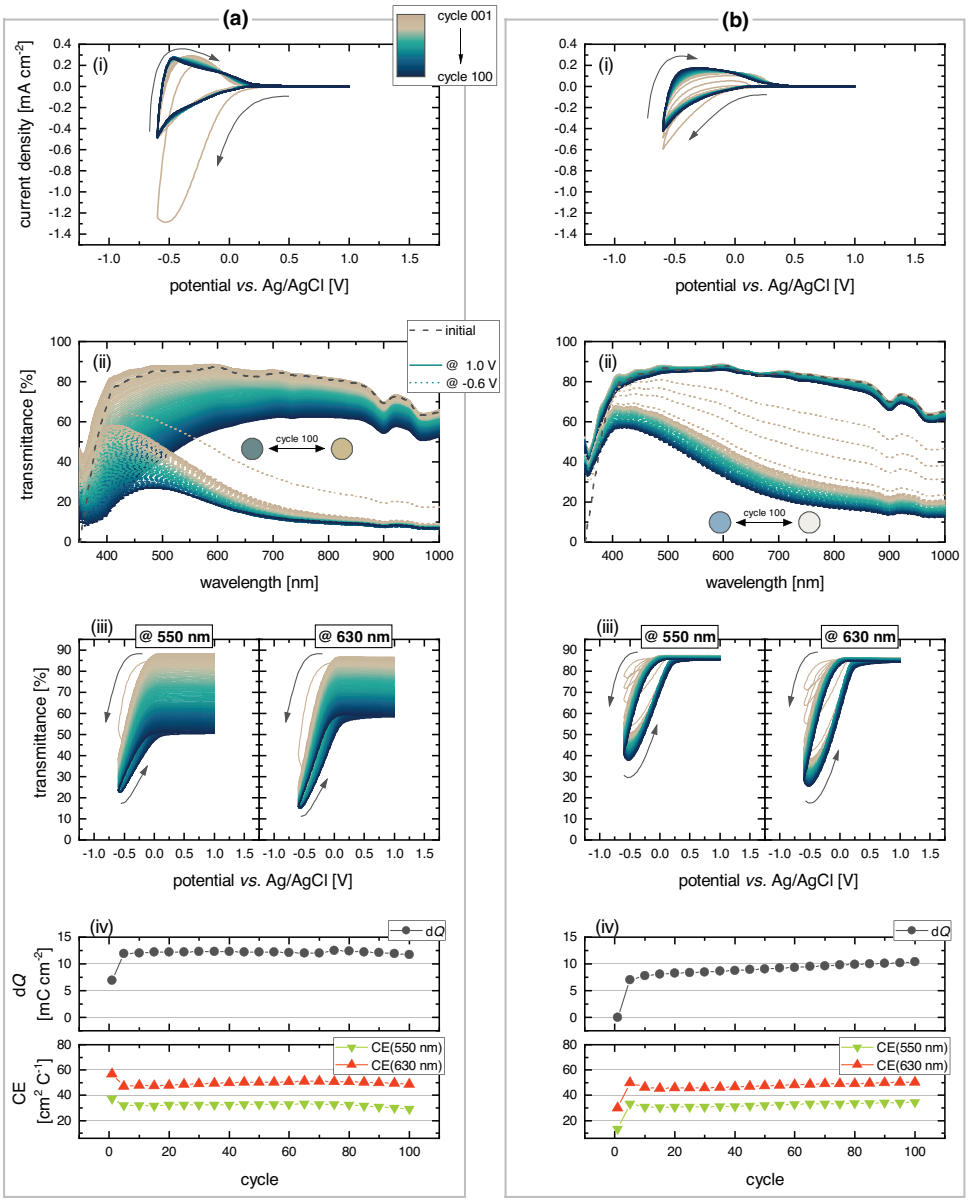

Figure 4. Spectro-electrochemical investigation on a) a pure a-WO_x sample and b) on the Al_2O_3|a-WO_x layer system, using 1 M $LiClO_4$ in PC with 10 vol% water as an electrolyte. i) The electrochemical properties are investigated over 100 CV cycles between –0.6 and 1.0 V. ii) The optical transmittance of the samples is shown for the initial state (dashed line) as well as for the intercalated (dotted line, at –0.6 V) and deintercalated state (solid line, at 1.0 V). iii) Simultaneously, the transmittance hysteresis at 550 and 630 nm is given for the entire measurement. iv) The charge density involved in the CV (upper plot) and the resulting coloration efficiency at 550 and 630 nm are shown for every 5th cycle (bottom plot).

4. Experimental Section

Tungsten oxide films were deposited by RF magnetron sputter deposition using a 4 in. W target from *Kurt J. Lesker Company* with a purity of 99.95%. The base pressure of the chamber was in the order of 10^{-7} mbar. The processes were performed with a power density of 1.2 W cm^{-2}. Reactive sputtering was performed using an argon–oxygen gas mixture. All a-WO_x samples shown here were grown with an O_2-gas flow of 20 sccm and an Ar-gas flow of 30 sccm. The purity of both gases was 99.999%. FTO (*Zhuhai Kaivo Optoelectronic Technology Co., Ltd.*) coated glass was used as substrate to ensure electrical contact for the electrochemical measurements.

The Al_2O_3 layers were prepared by atomic layer deposition using a *Picosun R200* Standard system of hot-wall design. Trimethylaluminum (TMA) and water were used as precursors without additional heating. The substrate temperature was set to 100 °C. In the first half cycle of the deposition process, a 0.5 s TMA pulse was introduced followed by a 0.5 s N_2 flush. Subsequently, water was introduced for 3 s and removed from the chamber by a 1 s N_2 flush. After performing 5 ALD cycles, Al_2O_3 films of about 0.75 nm thickness were obtained. The growth rate was determined by X-ray reflectometry measurements. The layer thickness was optimized in advance to ensure charge transfer of the ions used in the electrochemical treatment.

XPS (*PHI VersaProbe II*, Al K_α = 1486.6 eV) was used to study the material composition and obtain information on the electronic structure. The measurements are performed at a source angle of 45°. All electrochemically treated samples were pre-cleaned with anhydrous isopropanol before the XPS measurement. Charge neutralization

was achieved by a combination of an Ar^+- and an e^--gun. A common procedure of postcalibration referred to the use of the C 1s signal. At the same time, this was quite controversial, as there was often no accurate knowledge about the exact nature of this signal.[88–91] In this study, the postcalibration of the as-deposited sample was performed using the W $4f_{7/2}$ signal fixed at 35.6 eV, according to literature.[81–84] For electrochemically pretreated samples, two etching steps, each of 240 s, were performed in situ after studying the sample surface. Here, depth profiling was performed by argon ion etching with an accelerating voltage of 1 kV. In this process, the etching step induced preferential removal of oxygen and simultaneously produced reduced W species, as had already been reported for various metal oxides.[84,92,93] Therefore, formation of a metallic component could be observed already after two etching steps in the W 4*f* signal. The metallic W $4f_{7/2}$ component was used to set the postcalibration to 31.0 eV for electrochemically pretreated samples.

Spectro- and electrochemical analyses were performed using an IviumStat potentiostat from *IviumTechnologies*. For the electrochemical measurements, a PECC-2 type cell from *Zahner-Elektrik GmbH & Co. KG* was used in a three-electrode configuration. Here, the investigated layer system acted as the working electrode and a platinum wire served as the counter electrode. In addition, an Ag/AgCl reference electrode from *Innovative Instruments, Inc.* was used to which all voltages were referred to. The electrolyte used consisted of 1 M lithium perchlorate ($LiClO_4$, purity of 99.99%, *Sigma-Aldrich Chemie GmbH*) dissolved in propylene carbonate (PC, anhydrous, *Th. Geyer GmbH & Co. KG*). To study the influence of water on the electrochromic switching characteristic, a deionized water content of 10 vol% was admixed to the electrolyte. The CP was used for the insertion of a specific charge density into the working electrode by applying a constant cathodic current density of −0.65 mA cm^{-2} for a defined time. The deintercalation step, on the other hand, was performed using CA, in which a predefined voltage (here 1.5 V) was applied for a specified time. In this study, CV was used as the standard procedure for evaluating the electrochromic switching performance. The studies in nonaqueous electrolyte were performed using a potential range between −1.0 and 1.5 V. Using the aqueous electrolyte, the range under consideration was adjusted to −0.6 and 1.0 V. In both cases, the measurements were carried out using a sweep rate of 10 mV s^{-1}. To evaluate the electrochromic properties, optical measurements were carried out in operando using a MultiSpec SC-MCS CCD spectrometer (*tec5 AG*). The color impression of the electrochromic films shown here corresponded to the real optical color and was calculated from the measurement data of the spectrometer to RGB values using the D65 standard illumination according to reference.[94] To calculate the coloration efficiency CE, the wavelength-dependent transmittance of the intercalated (colored, T_c) and deintercalated (bleached, T_b) states yielded the optical density (ΔOD) divided by the charge density dQ involved per cycle:

$$CE = \frac{\Delta OD}{dQ} = \frac{\log_{10}\left(\frac{T_b}{T_c}\right)}{dQ} \quad (3)$$

Thus, a high coloration efficiency provided a large optical modulation with small charge transfer. Here, the coloration efficiency at wavelengths of 550 and 630 nm was evaluated.

Supporting Information

Supporting Information is available from the Wiley Online Library or from the author.

Acknowledgements

The authors thank T.H.Q. Nguyen and S. Göbel for fruitful discussions and valuable help in the experimental setup. The authors are grateful to E. Monte for the design and implementation of the graphical abstract. The work of M.G. and S.L.B. was funded by the DFG via the RTG (Research Training Group) 2204 "Substitute Materials for Sustainable Energy Technologies."

Open access funding enabled and organized by Projekt DEAL.

Conflict of Interest

The authors declare no conflict of interest.

Data Availability Statement

The data that support the findings of this study are available from the corresponding author upon reasonable request.

Keywords

atomic layer deposition, electrochromic device, protective layer, radio-frequency magnetron sputtering, tungsten oxide, X-ray photoelectron spectroscopy

Received: December 1, 2022
Revised: January 23, 2023
Published online: March 28, 2023

[1] bp, *Statistical Review of World Energy*, 70th ed. **2021**.
[2] *World population prospects*, United Nations, New York, NY, **2019**.
[3] C. Yuan, H. B. Wu, Y. Xie, X. W. D. Lou, *Angew. Chem., Int. Ed. Engl.* **2014**, *53*, 1488.
[4] S. Yuan, X. Duan, J. Liu, Y. Ye, F. Lv, T. Liu, Q. Wang, X. Zhang, *Energy Storage Mater.* **2021**, *42*, 317.
[5] Z. Lei, J. M. Lee, G. Singh, C. I. Sathish, X. Chu, A. H. Al-Muhtaseb, A. Vinu, J. Yi, *Energy Storage Mater.* **2021**, *36*, 514.
[6] W. Han, Q. Shi, R. Hu, *Nanomaterials* **2021**, *11*, 692.
[7] V. Rai, R. S. Singh, D. J. Blackwood, D. Zhili, *Adv. Eng. Mater.* **2020**, *22*, 2000082.
[8] A. S. Lakhnot, T. Gupta, Y. Singh, P. Hundekar, R. Jain, F. Han, N. Koratkar, *Energy Storage Mater.* **2020**, *27*, 506.
[9] D. Becker, M. Börner, R. Nölle, M. Diehl, S. Klein, U. Rodehorst, R. Schmuch, M. Winter, T. Placke, *ACS Appl. Mater. Interfaces* **2019**, *11*, 18404.
[10] M. Li, H. Yan, H. Ning, X. Li, J. Zhong, X. Fu, T. Qiu, D. Luo, R. Yao, J. Peng, *Appl. Syst. Innovation* **2022**, *5*, 60.
[11] J. Bentley, S. Desai, B. P. Bastakoti, *Chemistry* **2021**, *27*, 9241.
[12] X. Chen, J. Yang, Y. Cao, L. Kong, J. Huang, *ChemElectroChem* **2021**, *8*, 4427.
[13] W. Wu, M. Wang, J. Ma, Y. Cao, Y. Deng, *Adv. Electron. Mater.* **2018**, *4*, 1800185.
[14] C. G. Granqvist, M. A. Arvizu, İ. Bayrak Pehlivan, H.-Y. Qu, R.-T. Wen, G. A. Niklasson, *Electrochim. Acta* **2018**, *259*, 1170.
[15] G. A. Niklasson, C. G. Granqvist, *J. Mater. Chem.* **2007**, *17*, 127.
[16] Y. Ke, J. Chen, G. Lin, S. Wang, Y. Zhou, J. Yin, P. S. Lee, Y. Long, *Adv. Energy Mater.* **2019**, *9*, 1902066.
[17] P. Dong, G. Hou, X. Xi, R. Shao, F. Dong, *Environ. Sci.: Nano* **2017**, *4*, 539.
[18] H. Hemmelmann, J. K. Dinter, M. T. Elm, *Adv. Mater. Interfaces* **2021**, *8*, 2002074.
[19] D. H. Jackson, T. F. Kuech, *J. Power Sources* **2017**, *365*, 61.
[20] J.-T. Lee, F.-M. Wang, C.-S. Cheng, C.-C. Li, C.-H. Lin, *Electrochim. Acta* **2010**, *55*, 4002.

[21] J. Y. Seok, A. S. Cavanagh, Y. Yan, S. M. George, A. Manthiram, *J. Electrochem. Soc.* **2011**, *158*, A1298.
[22] Architecture 2030, Why the building sector? https://architecture2030.org/why-the-building-sector/ (accessed: January 2023).
[23] Energy efficiency in buildings. Greater focus on cost-effectiveness still needed. Special report, No 11, 2020. Publications Office of the European Union, Luxembourg, **2020**.
[24] C. G. Granqvist, *Thin Solid Films* **2014**, *564*, 1.
[25] S. K. Deb, *Appl. Opt.* **1969**, *8*, 192.
[26] S. K. Deb, *Philos. Mag.* **1973**, *27*, 801.
[27] C. Granqvist, *Electrochim. Acta* **1999**, *44*, 3005.
[28] C. Granqvist, *Sol. Energy Mater. Sol. Cells* **2000**, *60*, 201.
[29] T. van Nguyen, K. A. Huynh, Q. van Le, H. Kim, S. H. Ahn, S. Y. Kim, *Int. J. Energy Res.* **2021**, *45*, 8061.
[30] T. H. Q. Nguyen, F. Eberheim, S. Göbel, P. Cop, M. Eckert, T. P. Schneider, L. Gümbel, B. M. Smarsly, D. Schlettwein, *Appl. Sci.* **2022**, *12*, 2327.
[31] W. Cheng, E. Baudrin, B. Dunn, J. I. Zink, *J. Mater. Chem.* **2001**, *11*, 92.
[32] Y. Wang, Z. Meng, H. Chen, T. Li, D. Zheng, Q. Xu, H. Wang, X. Y. Liu, W. Guo, *J. Mater. Chem. C* **2019**, *7*, 1966.
[33] C. S. Blackman, I. P. Parkin, *Chem. Mater.* **2005**, *17*, 1583.
[34] A. Rougier, F. Portemer, A. Quédé, M. El Marssi, *Appl. Surf. Sci.* **1999**, *153*, 1.
[35] Y. S. Zou, Y. C. Zhang, D. Lou, H. P. Wang, L. Gu, Y. H. Dong, K. Dou, X. F. Song, H. B. Zeng, *J. Alloys Compd.* **2014**, *583*, 465.
[36] M. Gies, F. Michel, C. Lupó, D. Schlettwein, M. Becker, A. Polity, *J. Mater. Sci.* **2021**, *56*, 615.
[37] Y. Shi, M. Sun, Y. Zhang, J. Cui, X. Shu, Y. Wang, Y. Qin, J. Liu, H. H. Tan, Y. Wu, *ACS Appl. Mater. Interfaces* **2020**, *12*, 32658.
[38] S. S. Kalagi, S. S. Mali, D. S. Dalavi, A. I. Inamdar, H. Im, P. S. Patil, *Electrochim. Acta* **2012**, *85*, 501.
[39] S.-H. Lee, H. M. Cheong, C. E. Tracy, A. Mascarenhas, A. W. Czanderna, S. K. Deb, *Appl. Phys. Lett.* **1999**, *75*, 1541.
[40] S. Cong, F. Geng, Z. Zhao, *Adv. Mater.* **2016**, *28*, 10518.
[41] P. Gerard, A. Deneuville, G. Hollinger, T. M. Duc, *J. Appl. Phys.* **1977**, *48*, 4252.
[42] G. A. Niklasson, L. Berggren, A.-L. Larsson, *Sol. Energy Mater. Sol. Cells* **2004**, *84*, 315.
[43] T. J. Vink, E. P. Boonekamp, R. Verbeek, Y. Tamminga, *J. Appl. Phys.* **1999**, *85*, 1540.
[44] M. S. Burdis, J. R. Siddle, *Thin Solid Films* **1994**, *237*, 320.
[45] H.-H. Lu, *J. Alloys Compd.* **2008**, *465*, 429.
[46] Y.-S. Lin, Y.-L. Chiang, J.-Y. Lai, *Solid State Ionics* **2009**, *180*, 99.
[47] G. Atak, İ. Bayrak Pehlivan, J. Montero, C. G. Granqvist, G. A. Niklasson, *Electrochim. Acta* **2021**, *367*, 137233.
[48] A. V. Shchegolkov, S.-H. Jang, A. V. Shchegolkov, Y. V. Rodionov, A. O. Sukhova, M. S. Lipkin, *Nanomaterials* **2021**, *11*, 2376.
[49] J. Zhang, J. Tu, X. Xia, X. Wang, C. Gu, *J. Mater. Chem.* **2011**, *21*, 5492.
[50] C. Kim, V. Lokhande, D. Youn, T. Ji, *J. Solid State Electrochem.* **2022**, *26*, 1557.
[51] G. Atak, İ. Bayrak Pehlivan, J. Montero, D. Primetzhofer, C. G. Granqvist, G. A. Niklasson, *Mater. Today Proc.* **2020**, *33*, 2434.
[52] B.-R. Koo, K.-H. Kim, H.-J. Ahn, *Appl. Surf. Sci.* **2018**, *453*, 238.
[53] C.-T. Lee, D. Chiang, P.-K. Chiu, C.-M. Chang, C.-C. Jaing, S.-L. Ou, K.-S. Kao, *IEEE Trans. Magn.* **2014**, *50*, 1.
[54] G. Luo, L. Shen, J. Zheng, C. Xu, *J. Mater. Chem. C* **2017**, *5*, 3488.
[55] H. Najafi-Ashtiani, A. Bahari, S. Gholipour, *J. Mater. Sci.: Mater. Electron.* **2018**, *29*, 5820.
[56] M.-D. Peng, Y.-Z. Zhang, L.-X. Song, L.-N. Wu, Y.-L. Zhang, X.-F. Hu, *Surf. Eng.* **2017**, *33*, 305.
[57] K. Shen, K. Sheng, Z. Wang, J. Zheng, C. Xu, *Appl. Surf. Sci.* **2020**, *501*, 144003.
[58] J. Zhou, Y. Wei, G. Luo, J. Zheng, C. Xu, *J. Mater. Chem. C* **2016**, *4*, 1613.
[59] L. J. O.-R. de, A. DR, U. Pal, L. Castañeda, *Electrochim. Acta* **2011**, *56*, 2599.
[60] V. Madhavi, P. J. Kumar, P. Kondaiah, O. M. Hussain, S. Uthanna, *Ionics* **2014**, *20*, 1737.
[61] S. Xie, Z. Bi, Y. Chen, X. He, X. Guo, X. Gao, X. Li, *Appl. Surf. Sci.* **2018**, *459*, 774.
[62] T. C. Arnoldussen, *J. Electrochem. Soc.* **1981**, *128*, 117.
[63] O. Bohnke, C. Bohnke, G. Robert, B. Carquille, *Solid State Ionics* **1982**, *6*, 121.
[64] B. Reichman, A. J. Bard, *J. Electrochem. Soc.* **1979**, *126*, 583.
[65] N. Yoshiike, S. Kondo, *J. Electrochem. Soc.* **1983**, *130*, 2283.
[66] N. Yoshiike, S. Kondo, *J. Electrochem. Soc.* **1984**, *131*, 809.
[67] G. Leftheriotis, S. Papaefthimiou, P. Yianoulis, *Sol. Energy Mater. Sol. Cells* **2004**, *83*, 115.
[68] P. Judeinstein, R. Morineau, J. Livage, *Solid State Ionics* **1992**, *51*, 239.
[69] J.-G. Zhang, E. C. Tracy, D. K. Benson, S. K. Deb, *J. Mater. Res.* **1993**, *8*, 2649.
[70] J. S. Yun, J. Kim, T. Young, R. J. Patterson, D. Kim, J. Seidel, S. Lim, M. A. Green, S. Huang, A. Ho-Baillie, *Adv. Funct. Mater.* **2018**, *28*, 1705363.
[71] L. Zhang, M. G. EA, C.-W. Tai, K. Ł, H. Sommer, P. Novák, M. El Kazzi, S. Trabesinger, *ACS Appl. Mater. Interfaces* **2022**, *14*, 13240.
[72] G. He, J. Gao, H. Chen, J. Cui, Z. Sun, X. Chen, *ACS Appl. Mater. Interfaces* **2014**, *6*, 22013.
[73] J. Kim, J. W. Lim, G. Kim, M. Shin, *ACS Appl. Mater. Interfaces* **2021**, *13*, 4968.
[74] J.-H. Kim, E. Y. Choi, B.-J. Kim, E. Han, N. Park, *Vacuum* **2019**, *162*, 47.
[75] M. D. Groner, S. M. George, R. S. McLean, P. F. Carcia, *Appl. Phys. Lett.* **2006**, *88*, 051907.
[76] K. Leung, Y. Qi, K. R. Zavadil, Y. S. Jung, A. C. Dillon, A. S. Cavanagh, S.-H. Lee, S. M. George, *J. Am. Chem. Soc.* **2011**, *133*, 14741.
[77] H. T. Nguyen, M. R. Zamfir, L. D. Duong, Y. H. Lee, P. Bondavalli, D. Pribat, *J. Mater. Chem.* **2012**, *22*, 24618.
[78] Y. Liu, N. S. Hudak, D. L. Huber, S. J. Limmer, J. P. Sullivan, J. Y. Huang, *Nano Lett.* **2011**, *11*, 4188.
[79] S. C. Jung, Y.-K. Han, *J. Phys. Chem. Lett.* **2013**, *4*, 2681.
[80] Z. Zhang, L. Wu, D. Zhou, W. Weng, X. Yao, *Nano Lett.* **2021**, *21*, 5233.
[81] A. P. Shpak, A. M. Korduban, M. M. Medvedskij, V. O. Kandyba, *J. Electron Spectrosc. Relat. Phenom.* **2007**, *156–158*, 172.
[82] J. C. Dupin, D. Gonbeau, I. Martin-Litas, P. Vinatier, A. Levasseur, *J. Electron Spectrosc. Relat. Phenom.* **2001**, *120*, 55.
[83] V. I. Shapovalov, A. E. Lapshin, A. G. Gagarin, L. P. Efimenko, *Glass Phys. Chem.* **2014**, *40*, 553.
[84] F. Y. Xie, L. Gong, X. Liu, Y. T. Tao, W. H. Zhang, S. H. Chen, H. Meng, J. Chen, *J. Electron Spectrosc. Relat. Phenom.* **2012**, *185*, 112.
[85] C.-P. Li, R. C. Tenent, A. C. Dillon, R. M. Morrish, C. A. Wolden, *ECS Electrochem. Lett.* **2012**, *1*, H24.
[86] V. Raja, K. Hadiyal, A. K. Nath, L. R. Viannie, P. Sonar, J. Molina-Reyes, R. Thamankar, *Mater. Sci. Eng., B* **2021**, *264*, 114968.
[87] W. J. Lee, T.-Y. Cho, S.-H. Choa, S.-K. Cho, *Thin Solid Films* **2021**, *720*, 138524.
[88] G. Johansson, J. Hedman, A. Berndtsson, M. Klasson, R. Nilsson, *J. Electron Spectrosc. Relat. Phenom.* **1973**, *2*, 295.
[89] G. Greczynski, L. Hultman, *ChemPhysChem* **2017**, *18*, 1507.
[90] G. Greczynski, L. Hultman, *Prog. Mater. Sci.* **2020**, *107*, 100591.
[91] G. Greczynski, L. Hultman, *Angew Chem Int Ed Engl* **2020**, *59*, 5002.
[92] G. Silversmit, D. Depla, H. Poelman, G. B. Marin, G. R. de, *Surf. Sci.* **2006**, *600*, 3512.
[93] R. Simpson, R. G. White, J. F. Watts, M. A. Baker, *Appl. Surf. Sci.* **2017**, *405*, 79.
[94] C. Lupo, F. Eberheim, D. Schlettwein, *J. Mater. Sci.* **2020**, *55*, 14401.